



Nanoscale

Revisiting Pt/TiO₂ photocatalyst in the thermally assisted photocatalytic reduction of CO₂

Journal:	<i>Nanoscale</i>
Manuscript ID	NR-ART-11-2019-009743.R1
Article Type:	Paper
Date Submitted by the Author:	01-Feb-2020
Complete List of Authors:	<p>Yu, Fei; Northeast Normal University, Center for Advanced Optoelectronic Functional Materials Research Wang, Changhua; Northeast Normal University, Physics Ma, He; Northeast Normal University, Physics Song, Miao; Pacific Northwest National Laboratory Li, Dongsheng; Pacific Northwest National Laboratory, Li, Yingying; Northeast Normal University, Physics Li, Songmei; Northeast Normal University, Physics Zhang, Xintong; Northeast Normal University, Key Laboratory for UV-Emitting Materials and Technology of Ministry of Education Liu, Yichun; Northeast Normal University, Center for Advanced Optoelectronic Functional Materials Research</p>

SCHOLARONE™
Manuscripts

ARTICLE

Revisiting Pt/TiO₂ photocatalyst in the thermally assisted photocatalytic reduction of CO₂

Received 00th January 20xx,
Accepted 00th January 20xx

Fei Yu^a, Changhua Wang^{a*}, He Ma^a, Miao Song^b, Dongsheng Li^b, Yingying Li^a, Songmei Li^a, Xintong Zhang^{a*} and Yichun Liu^a

DOI: 10.1039/x0xx00000x

The artificial photosynthesis by semiconductor oxide photocatalysis is presently challenging due to low CO₂ conversion rates and poor product selectivity. To promote CO₂ reduction, Pt/TiO₂ has been deemed as a classical photocatalyst. In this work, we restudy Pt/TiO₂ in a case of thermally-assisted photocatalytic reduction of CO₂ and reveal a different story between photocatalysis and photothermal catalysis. By taking disordered Pt/TiO_{2-x} as an example, it is not impressive for CO₂ conversion via photocatalysis at 298 K. However, when the system temperature is increased to 393 K, CO₂ conversion rate is significantly enhanced by a factor of 155 referred to pristine TiO₂ and a high selectivity of CH₄ of 87.5% is surprisingly achieved. Thermal coupled photocatalysis discover a promoted evolution of H₂ side product over Pt (4.06 nm)/TiO₂ and whereas a promoted H₂ splitting over Pt (2.33 nm)/TiO₂, which is seldom observed in conventional Pt/TiO₂ photocatalysis. The synergy of improved charge separation at Pt/TiO_{2-x} interface induced by surface disordering and accelerated H₂ consumption nearby smaller Pt nanoparticles by thermal assistance are believed critically important for simultaneous enhancement of CO₂ conversion rates and CH₄ product selectivity. This study inspires revisiting not only Pt/TiO₂ but also reactivating other silent semiconductor oxide photocatalyst in thermal-assisted photocatalysis.

1. Introduction

The production of hydrocarbons from the photoreduction of CO₂ using semiconductor oxide photocatalysts is a promising approach for addressing the issues of both fossil-fuel depletion and global warming.^{1,2} In recent years, tremendous efforts have been devoted to searching for candidates to overcome the sluggish CO₂ conversion rate and the family of semiconductor oxide photocatalyst have been rapidly growing.^{3,4} Significant advance has been made in materials engineering for enhanced photocatalysis, such as heterojunction engineering,⁵ defect engineering,⁶ and so on.⁷⁻¹⁰ In the long-term of materials research and engineering, the thermal effect is deemed negligible and rarely considered for boosting photocatalysis. However, very recent studies highlight that thermal assistance remarkably enhance the CO₂ conversion rate over several semiconductor oxide.¹¹⁻¹³ It is highly anticipated to restudy photocatalyst as photothermal catalyst and uncover the veil of secrecy behind thermal coupled photocatalytic reduction of CO₂.

The past work has demonstrated that loading of Pt nanoparticles on TiO_{2-x} supports (i.e., Pt/TiO_{2-x}) offers significant potential for enabling high CH₄ selectivity in standard photocatalytic CO₂ reduction processes.¹⁴ Here, the oxygen vacancies in TiO_{2-x} have

been shown to promote the wide dispersion and size reduction of Pt nanoparticles deposited via a photochemical route. Moreover, electrons trapped at oxygen vacancies are more likely released to the surface of the catalyst by thermal activation, and hence the process of CO₂ reduction on the catalyst surface is accelerated.¹⁵⁻¹⁷ However, our recent study of the thermally coupled photoreduction of CO₂ with H₂O using TiO_{2-x} revealed that oxygen vacancies enhanced the rate of CO evolution from CO₂ conversion, which involves the transfer of two electrons, rather independently of the evolution rates of other products involving a greater number of transferred electrons.¹⁸ Other studies have reported similar results (Table S1). As such, increasing the CH₄ selectivity of thermally coupled photocatalysis processes using TiO₂ is not expected to be achieved solely by the introduction of oxygen vacancies. The Pt nanoparticles not only facilitate the separation of electrons and holes, and promote the transfer of multiple electrons, but also act as atomic hydrogen reservoirs that supply sufficient and readily available protons for CH₄ formation.¹⁹⁻²¹ On considering the consistently reported enhanced photocatalytic performance for CO₂ reduction, Pt/TiO_{2-x} serves as an ideal model to be restudied as photothermal catalyst, which would stimulate broad interest on other semiconductor oxides photocatalyst for photothermal catalysis.

On restudying Pt/TiO_{2-x} photocatalyst for thermal-assisted photocatalytic reduction of CO₂ with H₂O, two competitions between photocatalysis and thermal-assisted photocatalysis should be taken into consideration. Firstly, as stated above, Pt/TiO₂ can promote charge separation in photocatalysis. However, the imposed thermal energy in thermal-assisted photocatalysis can result in serious electron-hole recombination due to the enhanced random thermal motion of the charge carriers. Secondly, from a thermodynamics

^a Key Laboratory of UV-Emitting Materials and Technology of Chinese Ministry of Education, Northeast Normal University, 5268 Renmin Street, Changchun 130024, China. E-mail: wangch100@nenu.edu.cn; xtzhang@nenu.edu.cn

^b Physical and Computational Sciences Directorate, Pacific Northwest National Laboratory, Richland, WA, 99352, United States

†Electronic Supplementary Information (ESI) available: [details of any supplementary information available should be included here]. See DOI: 10.1039/x0xx00000x

standpoint, an increasing reaction temperature tends to move the step-reaction of H_2O splitting forward due to the nature of endothermic reaction ($\Delta H > 0$). Combining the role of Pt cocatalyst to promote H_2 evolution as reported elsewhere,^{22–24} there will be a positive effect of thermal on the photocatalytic H_2O splitting over $\text{Pt}/\text{TiO}_{2-x}$. Despite this, the followed CO_2 hydrogenation for CH_4 product is an exothermic reaction ($\Delta H < 0$), an increasing reaction temperature tends to move the step-reaction of CO_2 hydrogenation backward. With this regard, thermal will impose a negative effect on photocatalytic CO_2 reduction. On concerning above two competitions between photocatalysis and thermal-assisted photocatalysis, it is highly required that the $\text{Pt}/\text{TiO}_{2-x}$ interface be more precisely designed and engineered than when applied in standard photocatalysis.

Charge carrier recombination in reactions photocatalyzed by TiO_2 has been demonstrated to be reduced by the introduction of disorder at the surface of the photocatalyst.^{25–27} In addition to promoting charge carrier separation, surface disorder has been demonstrated to extend the range of visible light absorption of the photocatalyst relative to standard TiO_2 .^{28,29} However, while this approach offers substantial potential for use in thermally assisted photocatalysis processes based on $\text{Pt}/\text{TiO}_{2-x}$ photocatalysts, this approach has not been applied for the photoreduction of CO_2 .

The present work addresses the above discussed issues regarding thermally assisted photocatalysis processes using $\text{Pt}/\text{TiO}_{2-x}$ photocatalysts by inducing disorder in the surface layer of TiO_{2-x} using a high-power ultrasonic treatment. In addition to promoting charge carrier separation and extending the range of visible light absorption of the photocatalyst, the surface layer in the disordered TiO_{2-x} (D- TiO_{2-x}) is found to also play a key role in narrowing the size distribution of Pt nanoparticles, which are very important factors for enhancing the CO and the CH_4 evolution rates in the thermally coupled photocatalytic process. First, the electronic structure and CO_2 reduction mechanism of the pristine TiO_2 surface are investigated by density functional theory (DFT) calculations. Then, the performance of the thermally assisted photocatalytic process using the proposed $\text{Pt}/\text{D-TiO}_{2-x}$ photocatalyst for the reduction of CO_2 with H_2O and the formation of CH_4 is evaluated experimentally. The CH_4 evolution rate is observed to increase by a factor of approximately 71 as the reaction temperature is increased from 298 K to 393 K, and a high CH_4 selectivity of 87.5% is obtained. Moreover, the CH_4 formation rate obtained using the $\text{Pt}/\text{D-TiO}_{2-x}$ photocatalyst at 393 K is greater than that obtained using $\text{Pt}/\text{TiO}_{2-x}$ and TiO_{2-x} photocatalysts at 298 K by factors of approximately 100 and 155, respectively. The reasons for the superior thermally assisted photocatalytic performance of the proposed $\text{Pt}/\text{D-TiO}_{2-x}$ photocatalyst are discussed in detail.

2. Experimental

2.1 Fabrication of TiO_{2-x} nanoparticles

We prepared mixed-phase TiO_{2-x} nanoparticles by a hydrothermal method. This resulted in the production of a light-yellow powder. The target phases were anatase ($\text{TiO}_2(\text{A})$) and $\text{TiO}_2(\text{B})$. These target phases were adopted due to the fact that $\text{TiO}_2(\text{A})/\text{TiO}_2(\text{B})$ interfaces are better at suppressing charge

recombination than anatase/rutile interfaces.³⁰ In addition to the formation of mixed phases, oxygen vacancies can be naturally introduced in this step. The formation of TiO_{2-x} and D- TiO_{2-x} photocatalysts are illustrated in Scheme S1.

2.2 Ultrasonication treatment

We dispersed 0.5 g of the TiO_{2-x} nanoparticles into 100 mL of deionized water, and placed the solution in an XH-300 UL ultrasonic excitation apparatus (Beijing Xianghu Science and Technology Development Co., Ltd., China). This apparatus provides ultra-powerful ultrasonication with effects extending well beyond the dispersion of nanoparticles associated with standard ultrasonication.^{31,32} Here, ultra-powerful ultrasonication generates minute bubbles around the ultrasonic probe that can produce instantaneous temperatures as great as 5000 °C and extremely high pressures as great as 500 atmospheres, which are conditions that are sufficient to break chemical bonds at the surfaces of nanoparticles.^{33,34} The ultrasonic process was conducted for 8 h in the 1:1 pulse mode at a power of 1500 W and a frequency of 25 kHz. The ultrasonic process was controlled a titanium alloy ultrasonic probe inserted into the solution. After ultrasonic treatment, the powder was collected and dried in air at 80 °C. The colour of the resulting D- TiO_{2-x} powder was blue-grey. This blue-grey colour can be maintained for several months under ambient conditions.

2.3 Photodeposition of Pt on TiO_{2-x} and D- TiO_{2-x}

We dispersed 50 mg of TiO_{2-x} or D- TiO_{2-x} with 50 μL of $\text{H}_2\text{PtCl}_6 \cdot 6\text{H}_2\text{O}$ (1 wt.%) in a solution containing methanol (10 mL) and deionized water (90 mL). Dissolved oxygen was removed by bubbling N_2 gas into the mixture for 15 min. Then, the mixture was irradiated under full spectrum radiation for 1 h using a 300 W Xe lamp with constant stirring. Finally, the obtained products were collected by centrifugation and washed with water. The formation of $\text{Pt}/\text{TiO}_{2-x}$ and $\text{Pt}/\text{D-TiO}_{2-x}$ photocatalysts are also illustrated in Scheme S1.

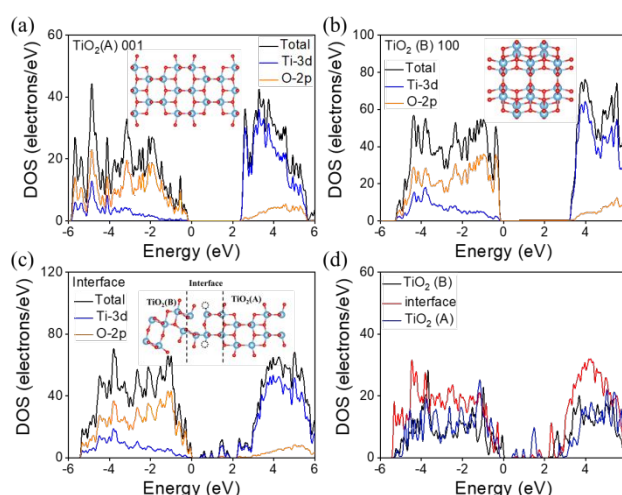


Fig. 1 Density of states (DOS) for (a) the (001) plane of $\text{TiO}_2(\text{A})$, (b) the (100) plane of $\text{TiO}_2(\text{B})$, and (c)-(d) the $\text{TiO}_2(\text{A})/\text{TiO}_2(\text{B})$ interface.

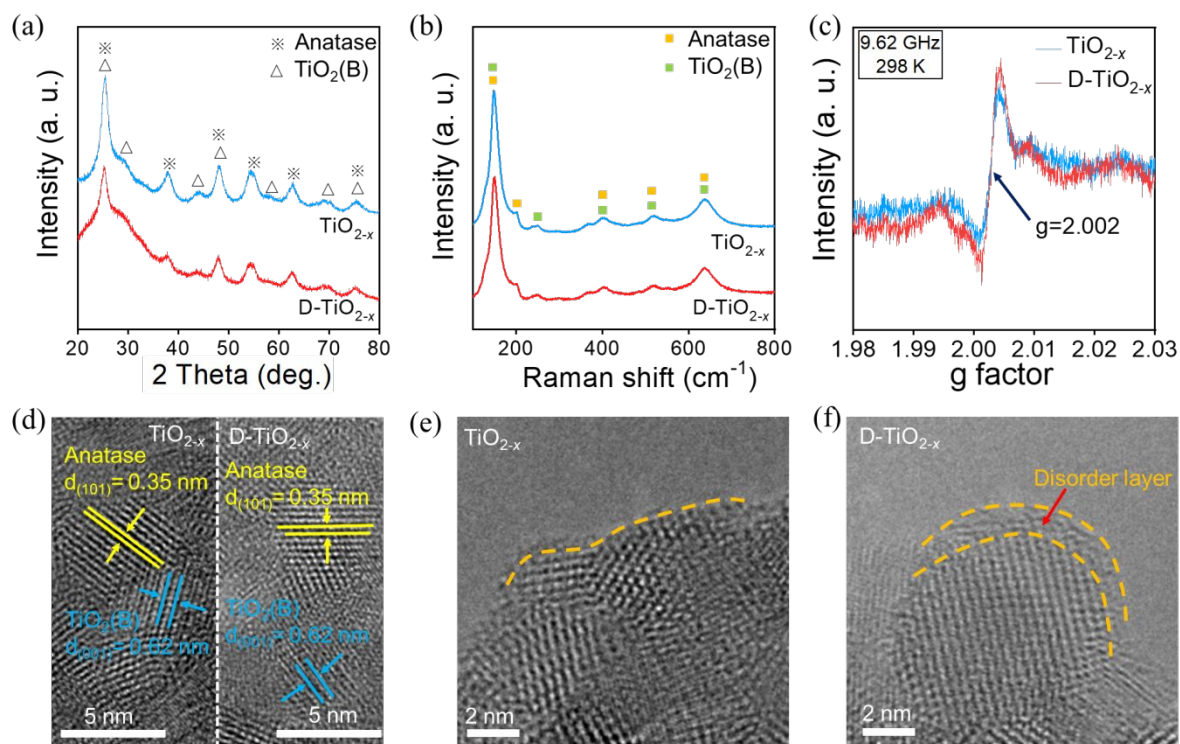


Fig. 2 Characterizations of the TiO_{2-x} and D-TiO_{2-x} photocatalysts: (a) XRD patterns; (b) Raman spectra; (c) ESR spectra; (d)–(f) HRTEM images.

3. Results and Discussion

3.1 Density functional theory results.

We first examined the electronic structures of the $\text{TiO}_2(\text{A})$ and $\text{TiO}_2(\text{B})$ supercells without oxygen vacancies, as respectively illustrated in the insets of Figs. 1a and b. These subfigures also present the obtained density of states (DOS) for the $\text{TiO}_2(\text{A})$ and $\text{TiO}_2(\text{B})$ models, respectively. The results indicate that the valence and conduction states are derived mainly from the O 2p and Ti 3d orbitals, respectively. In addition, the band structure exhibits no mid-gap states in the absence of oxygen vacancies. However, the DOS results shown in Fig. 1c based on the modelled $\text{TiO}_2(\text{A})/\text{TiO}_2(\text{B})$ interface with oxygen vacancies (inset of Fig. 1c) exhibits mid-gap electronic states below the conduction band. The results indicate that these can be mainly attributed to the Ti 3d orbitals. The individual roles contributed by $\text{TiO}_2(\text{A})$, $\text{TiO}_2(\text{B})$, and the $\text{TiO}_2(\text{A})/\text{TiO}_2(\text{B})$ interface for generating the mid-gap electronic states are illustrated in Fig. 1d, which demonstrates that all components have a significant effect on the charge carriers. Song and co-workers reported that the surface junction can promote the photogenerated carrier separation and offer more strongly reductive electrons for the photoreduction reaction or more strongly oxidative holes for the photooxidation reaction.³⁵ Accordingly, the $\text{TiO}_2(\text{A})/\text{TiO}_2(\text{B})$ structure with oxygen vacancies is shown to introduce mid-gap electronic states that can extend the wavelength range of light absorption and enhance the lifetimes of charge carriers. Wang and co-workers also demonstrated that the oxygen vacancies had two important roles: enhancing the charge carriers and adsorbing reactants easily.³⁶

The role of Pt loading on TiO_{2-x} in CO_2 reduction was also evaluated using DFT calculations.³⁷ Fig. S1 shows the total energy difference between the products and the reactants of each elementary step of

the overall reduction reaction when employing the TiO_{2-x} and $\text{Pt}/\text{TiO}_{2-x}$ photocatalysts. The results indicate that the CO_2 adsorption and the further reduction to CO over $\text{Pt}/\text{TiO}_{2-x}$ is superior than that of TiO_{2-x} , which is the rate limiting step in the entire reaction process. Thus, $\text{Pt}/\text{TiO}_{2-x}$ can greatly enhance the efficiency of CO_2 reduction.

3.2 Structure of TiO_{2-x} and D-TiO_{2-x}

The XRD patterns shown in Fig. 2a indicate the formation of mixed phases of $\text{TiO}_2(\text{A})$ (PDF#21-1272) and $\text{TiO}_2(\text{B})$ (PDF#46-1237) in both TiO_{2-x} and D-TiO_{2-x} . The Raman spectra of the TiO_{2-x} and D-TiO_{2-x} samples shown in Fig. 2b exhibit vibration modes at 147, 201, 400, 517, and 636 cm^{-1} characteristic of both $\text{TiO}_2(\text{A})$ and $\text{TiO}_2(\text{B})$ phases.³⁸ In addition, the peaks at 220 and 246 cm^{-1} are respectively attributable to $\text{TiO}_2(\text{A})$ and $\text{TiO}_2(\text{B})$, which further confirms the mixed phase composition of the samples. The ESR spectra of the TiO_{2-x} and D-TiO_{2-x} samples shown in Fig. 2c present a single signal peak at $g = 2.002$, demonstrating the presence of oxygen vacancies in the samples.³⁹ The signal intensity of ESR for TiO_{2-x} has a little enhancement compared with D-TiO_{2-x} which indicates the concentration of oxygen vacancies enhanced by the ultrasonication treatment.²⁸ The TEM image in Fig. S2a shows that the TiO_{2-x} sample consists of uniformly sized nanoparticles with an average diameter of 5 nm. The HRTEM images given in Fig. 2d for TiO_{2-x} and D-TiO_{2-x} clearly show interplanar spacing values of $d = 0.62$ nm and $d = 0.35$ nm, corresponding to the (001) facets of $\text{TiO}_2(\text{B})$ and the (101) facets of $\text{TiO}_2(\text{A})$, respectively, both before and after ultrasonic treatment. We also note that the applied ultrasonic treatment induces no obvious changes in the $\text{TiO}_2(\text{A})$ and $\text{TiO}_2(\text{B})$ crystalline phases (Figs. 2a and b). Moreover, the ultrasonic treatment is observed to have no effect on the nanoparticle morphology (Figs. S2a and d). Comparison of Figs. 2e and f (Figs. S3 and S4) show the presence of a disordered

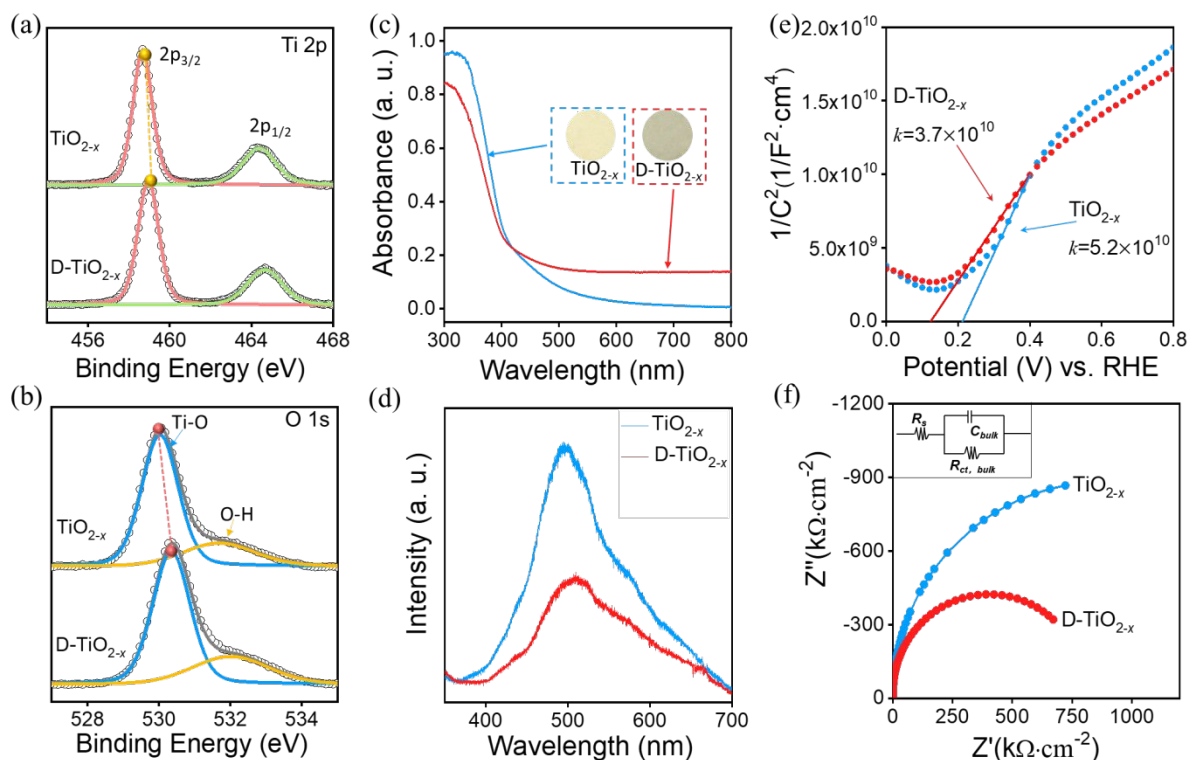


Fig. 3 Characterizations of the TiO_{2-x} and D-TiO_{2-x} photocatalysts: XPS spectra of (a) the Ti 2p doublet states and (b) the O 1s states; (c) UV-vis spectra, where the insets present photographs of respective samples employed during testing; (d) PL emission spectra obtained under 325 nm excitation; (e) Mott-Schottky plots obtained at a frequency of 1 kHz in the absence of incident light; (f) Nyquist plots obtained under illumination with a 1 M NaOH electrolyte at a DC potential of 1.23 V relative to a reversible hydrogen electrode (RHE) and an AC voltage amplitude of 10 mV with frequencies ranging from 100 kHz to 0.01 Hz, where the inset presents the equivalent circuit model employed during analysis.

surface layer on the crystalline core of TiO_{2-x} . Moreover, the straight lattice lines of the $\text{TiO}_2(\text{A})$ and $\text{TiO}_2(\text{B})$ crystallites are respectively bent at the edge of the nanoparticle in Fig. 2f and S4, demonstrating deviation from the standard crystalline structure of the phases at the outer layer. For our as-synthesized TiO_{2-x} , it should be admitted that the pre-existence of oxygen vacancy also contributes to disordered surface, as confirmed by the vague and disorder appearance edge (shown in Fig. 2e). On careful comparison between the disordered degree of TiO_2 before and after ultrasonic treatment (Fig. 2e vs Fig. 2f), the disordered degree is indeed enhanced. So, above results verify that the as-adopted ultrasonic treatment successfully creates disorder on the TiO_{2-x} nanoparticle surfaces.

Subtle structure changes in the TiO_{2-x} photocatalyst after ultrasonication treatment can be evaluated from a comparison of the XPS results for the Ti 2p doublet and O 1s states of the photocatalyst obtained before and after treatment, as shown in Figs. 3a and b, respectively. From the fitted peaks in Fig. 3a, we note that the binding energies corresponding to the $2p_{3/2}$ and $2p_{1/2}$ states of the Ti 2p doublet are 458.75 and 464.38 eV, respectively, which are indicative of a valence state of Ti^{4+} .⁴⁰ In addition, the binding energies of the Ti 2p states are observed to shift to higher values uniformly after ultrasonication. From Fig. 3b, the O 1s spectrum of TiO_{2-x} is deconvoluted to a single main peak located at 530.04 eV and a shoulder peak at 531.68 eV that respectively correspond to O-Ti and O-H surface hydroxyls.⁴¹ As observed for the O 1s states, the binding energies shift to higher values after ultrasonication. It is believed that the shift to a higher value of binding energy of the Ti 2p and O 1s

states could be attributed to the increased concentration of surface O vacancies, which is consistent with the results of ESR spectra.⁴² In addition, the ratios of the areas under the deconvoluted O 1s peaks representative of O-Ti and OH (i.e., $A_{\text{O-Ti}}/A_{\text{OH}}$) for TiO_{2-x} and D-TiO_{2-x} were calculated to be 0.33 and 0.40, respectively, indicating that the disordering process tends to increase the concentration of OH groups on the surface of TiO_{2-x} , as reported elsewhere.^{29,43} The combined results of HRTEM images and XPS clearly demonstrate that the ultrasonic treatment of TiO_{2-x} produces measurable disorder in the top surface layer.

The UV-vis diffuse absorbance spectra of the TiO_{2-x} and D-TiO_{2-x} powders are shown in Fig. 3c. Here, we note that the range of optical absorbance for TiO_{2-x} is extended from about 380 nm for standard TiO_2 to about 600 nm, which is induced by the oxygen vacancies introduced in the synthesis process.^{39,44} In addition, a comparison of the TiO_{2-x} and D-TiO_{2-x} spectra in the UV region indicates that the D-TiO_{2-x} spectrum leading to maximum absorbance increases at a smaller rate than that of the TiO_{2-x} spectrum, and that ultrasonication introduces a blue shift in the UV portion of the absorbance spectrum. The smaller slope correlates with decreased crystallinity, which can be associated with the disordered layer of D-TiO_{2-x} .⁴² The blue shift can be explained by the Moss-Burstein effect.^{45,46} Here, the Fermi level is shifted upward when the electron carrier concentration exceeds the DOS at the conduction band edge, which usually corresponds to degenerate doping in semiconductors. However, we can deduce from the DOS results presented in Fig. 1 that the lattice disorder generated by the $\text{TiO}_2(\text{A})/\text{TiO}_2(\text{B})$ interface in

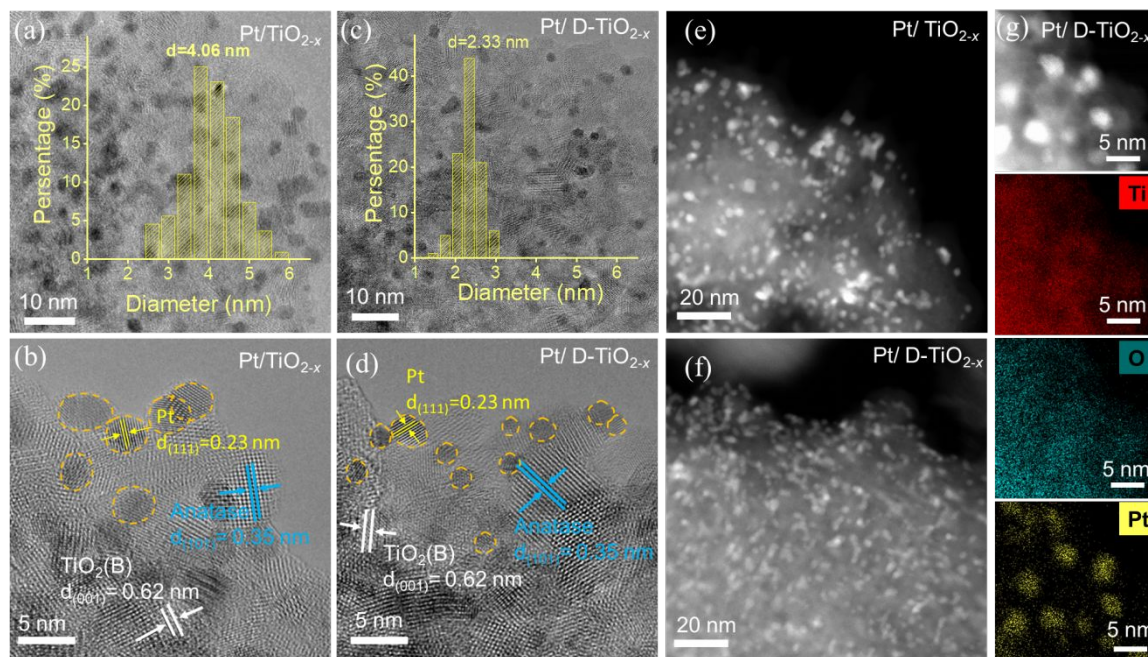


Fig. 4 Imaging results for Pt loaded TiO_{2-x} and D-TiO_{2-x} supports: (a), (c) HRTEM images, where the insets present histograms of the Pt particle size frequency distributions; (b), (d) higher magnification HRTEM images showing the interplanar spacing values of the various components and phases; (e), (f) HAADF-STEM images; (g) HAADF-STEM image of Pt/D-TiO_{2-x} and its corresponding elemental mappings for Pt, Ti, and O.

conjunction with oxygen vacancies introduces mid-gap states and forms a continuum of energy levels extending to the conduction band edge, which thereby results in an upward shift in the Fermi level.

The separation of photo-generated electrons and holes is readily evaluated according to the PL emission spectra of the materials because the probability of recombination between photogenerated electron-hole pairs is proportional to the PL emission intensity.⁴⁷ According to the PL emission spectra of the TiO_{2-x} and D-TiO_{2-x} materials shown in Fig. 3d, we note that the peak PL intensity of D-TiO_{2-x} is much less than that of TiO_{2-x} in the wavelength range of 350–700 nm. This clearly indicates that the disordered layer in the D-TiO_{2-x} photocatalyst reduces the probability of charge carrier recombination in TiO_{2-x} . This issue was further explored by analyses of the Mott-Schottky and EIS (Nyquist plots) results for the TiO_{2-x} and D-TiO_{2-x} photocatalysts shown in Figs. 3e and f, respectively. The results in Fig. 3e indicate that the slope of the Mott-Schottky plot for the D-TiO_{2-x} electrode was substantially less than that of TiO_{2-x} , revealing higher charge carrier densities for D-TiO_{2-x} than for TiO_{2-x} .^{48,49} This clearly indicates that the disordering process effectively improves the charge carriers of TiO_{2-x} . Similarly, the Nyquist plots shown in Fig. 3f indicate that the D-TiO_{2-x} electrode obtains a smaller charge-transfer resistance (R_{ct}) than that of TiO_{2-x} based on the equivalent circuit model shown in the inset of the figure, which further verifies that the disordering process effectively improves the charge transport characteristics of TiO_{2-x} .⁵⁰ The PL emission spectra coupled with the results of the Mott-Schottky and EIS analysis confirm that the disordered layer in TiO_{2-x} promotes charge carrier separation.

3.3 Pt loaded TiO_{2-x} and D-TiO_{2-x} supports

In addition to TEM images (Fig. S5), we present HRTEM images in Figs. 4a–d of Pt/TiO_{2-x} and Pt/D-TiO_{2-x} nanoparticles. These figures

clearly indicate that Pt nanoparticles are loaded on both TiO_{2-x} and D-TiO_{2-x} without agglomeration. The particle size distributions of the loaded Pt particles are included as insets within Figs. 4a and c, which indicate that the Pt particles loaded on TiO_{2-x} were 2.5–6 nm in diameter with an average diameter of 4.06 nm, while those loaded on D-TiO_{2-x} were 1.5–3.1 nm in diameter with an average diameter of 2.33 nm. As such, we can conclude that the Pt loaded on D-TiO_{2-x} had a narrower size distribution and smaller average size than that loaded on TiO_{2-x} . In other words, the disordered degree after high-power ultrasonic treatment can be obviously enhanced and substantially helps the decreasing of Pt size on TiO_2 surface. In addition, the higher magnification HRTEM images shown in Figs. 4b and d indicate that the interplanar spacing of the loaded Pt particles along the (111) plane are 0.23 nm, and that the Pt loading does not affect the *d*-spacing of the TiO_{2-x} and D-TiO_{2-x} supports (compare with Fig. 2). The HAADF-STEM images shown in Figs. 4e and f also demonstrate that the Pt particles on the D-TiO_{2-x} surface are smaller and more uniform than those on TiO_{2-x} . Elemental mapping was further conducted for D-TiO_{2-x} based on the HAADF-STEM image at the top of Fig. 4g to determine the distributions of the elemental components. As can be seen, elemental Pt was uniformly distributed on the D-TiO_{2-x} surface. We can conclude that the narrower particle size distribution and smaller average particle size obtained by D-TiO_{2-x} is the result of its disordered surface layer because this is the only significant difference between the two materials. Moreover, the loading of Pt nanoparticles by photodeposition suggests that the disordered surface layer of D-TiO_{2-x} generates a more photoactive surface than that of TiO_{2-x} . This is supported by the improved charge carrier separation obtained by the disordered surface layer of D-TiO_{2-x} , as discussed above.

XPS analysis was conducted to investigate the valance states of loaded Pt nanoparticles and changes in the chemical environments of Ti and O for TiO_{2-x} and D-TiO_{2-x} before and after Pt loading. As

shown in Fig. 5a, the high resolution Pt spectrum obtained for the $4f_{7/2}$ and $4f_{5/2}$ states can be deconvoluted into two peaks with

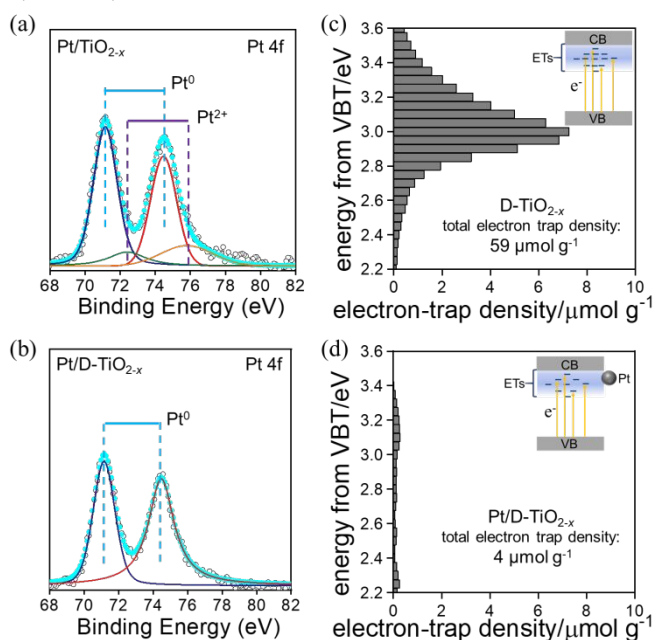


Fig. 5 XPS spectra of the Pt 4f doublet states of (a) Pt/TiO_{2-x} and (b) Pt/D-TiO_{2-x}. (c) RDB-PAS results for Pt/TiO_{2-x} and Pt/D-TiO_{2-x}. Here, the numbers such as <59> denote the total density of electron-traps (ETs) in units of $\mu\text{mol}\cdot\text{g}^{-1}$, and the inset provides a schematic illustrating the RDB-PAS process, where electrons are excited from the valance band (VB) to ETs lying below the conduction band (CB). (d) ESR spectra of Pt/TiO_{2-x} and Pt/D-TiO_{2-x}.

binding energies of 71.13 and 74.45 eV representative of Pt⁰ and Pt²⁺, respectively.⁵¹ However, the high resolution Pt spectrum shown in Fig. 5b for Pt/D-TiO_{2-x} provides single Gaussian peaks for the $4f_{7/2}$ and $4f_{5/2}$ states that are representative of Pt⁰. In addition, the high resolution O 1s and Ti 2p spectra obtained for TiO_{2-x} and Pt/TiO_{2-x} (Fig. S6) indicate that these peaks shift to higher binding energies after Pt loading. This may be the result of interactions between Pt²⁺ and O atoms. In contrast, the O 1s and Ti 2p peaks obtained for D-TiO_{2-x} exhibit no shifts after Pt loading. Consequently, the loaded Pt atoms on D-TiO_{2-x} were completely reduced to metallic Pt whereas a small percentage of the loaded Pt atoms on the TiO_{2-x} surface were not. These results further support that D-TiO_{2-x} provides superior photoactivity relative to that of TiO_{2-x}.

The RDB-PAS technology developed by Ohtani et al.^{52,53} can successfully measure the energy-resolved distribution of electron traps (ERDT) and provide valuable information regarding the density of electron traps (ETs) in materials based on the energy distribution of electron transitions from the top of the valance band (VBT) to existing ETs. As shown in Fig. 5c-d, the RDB-PAS characterization displays that electron trap density is decreased from 59 $\mu\text{mol}\cdot\text{g}^{-1}$ for D-TiO_{2-x} to 4 $\mu\text{mol}\cdot\text{g}^{-1}$ for Pt/D-TiO_{2-x}. This definitely demonstrates a decrease of surface defects after Pt loading. However, on further characterization by ESR, a subtle decrease of oxygen vacancy related ESR signal is observed in Fig. S7. The subtle decreased ESR signal seems not consistent with the significantly decreased electron trap density. After repeated ESR characterization, the subtle decreased ESR signal is confirmed. Accordingly, we tentatively deduce that the

disorder defect in D-TiO_{2-x} is only partly contributed by oxygen vacancy. The diminishing of other defects in addition to oxygen vacancy by Pt filling can not be detected by ESR. In fact, this hypothesis can be also supported by comparison on characterization results of D-TiO_{2-x} and TiO_{2-x}. As shown in ESR characterization in Fig. 2c, there is a subtle increased oxygen vacancy related ESR signal in D-TiO_{2-x} than TiO_{2-x} in spite of introducing disordered layer. However, a noticeable shift of binding energy of Ti 2p and O 1s in high resolution XPS spectra of D-TiO_{2-x} than TiO_{2-x}, which is frequently observed in other disordering engineered semiconductor oxides (Fig. 3a-b). Again, the sharp contrast between subtle increased ESR signal and significant XPS shift suggests that the disorder in D-TiO_{2-x} is partly contributed by oxygen vacancy.

3.4 Catalytic CO₂ reduction using TiO_{2-x} and D-TiO_{2-x} before and after Pt loading

3.4.1 CO yield before Pt loading. The results of PC and PTC induced CO₂ to CO conversion using the TiO_{2-x} and D-TiO_{2-x} photocatalysts are shown in Fig. S8 and Table 1. Here, CO and CH₄ were the main reduction products for both photocatalysts in both processes, while O₂, as an oxidation product, was undetected. This may be owing to the low sensitivity of the TCD used for the detection of O₂. We note from the figures that the formation rates of CO using the D-TiO_{2-x} photocatalyst were greater than that obtained using TiO_{2-x} at both 298 K (i.e., PC reduction) and 393 K (i.e., PTC reduction). In detail, the CO formation rate obtained during PC reduction using D-TiO_{2-x} was greater than that obtained using TiO_{2-x} by a factor of 1.51, while the CO formation rate obtained during PTC reduction using D-TiO_{2-x} was greater than that obtained using TiO_{2-x} by a factor of 1.83. Moreover, the CO formation rate obtained during PTC reduction using D-TiO_{2-x} was notably greater than that obtained during PC reduction using TiO_{2-x} by a factor of 230.3. This indicates that the D-TiO_{2-x} photocatalyst provides a particularly increased activity when coupled with thermal energy. However, the results in Fig. S8 show that the CH₄ yield is less than that of CO, and that this difference increases when the reduction process adopts the D-TiO_{2-x} photocatalyst, as well as, in particular, when it is coupled with thermal energy. These results demonstrate that the proposed disordering in the D-TiO_{2-x} photocatalyst is detrimental to the CH₄ yield, particularly when coupled with thermal energy.

In order to explore the effect of ultrasonication treatment, we study the effects of time of ultrasonic treatments on the photothermal-catalytic activity and properties of TiO_{2-x}. We treated TiO_{2-x} for 4, 8 and 12 hours, respectively (named US-X, X=4, 8 and 12, respectively). As shown in Fig.S9, the photothermal catalytic activity toward CO₂ reduction with H₂O was tested. The photothermal-catalytic results showed a volcanic trend with the increase of time of ultrasonication treatment. The TiO_{2-x} treated for 8 hours showed the highest CO yield. To understand the difference between photothermal activity of US-X, Mott-Schottky and EIS (Nyquist plots) analysis were performed and shown in Figs. S10. The results in Fig. S10a indicate that the slope of the Mott-Schottky plot sequence for tested samples is US-8 h > US-4 h > US-12 h > US-0 h, revealing highest charge carrier densities for US-8 h. This clearly indicates that the disordering process effectively improves the charge carriers of TiO_{2-x}. Similarly, the Nyquist plots shown in Fig. S10b indicate that the US-8

h electrode obtains a smallest charge-transfer resistance (R_{ct}) than that of US-4 h, US-12 h and US-0 h, which further verifies that the

Table 1 Characteristics of photocatalytic and photothermal catalytic induced CO_2 conversion processes using different photocatalysts.

Catalysts	Photocatalysis ^a			Photothermal catalysis ^a				
	CO yield ($\mu\text{mol}\cdot\text{h}^{-1}$)	CH_4 yield ($\mu\text{mol}\cdot\text{h}^{-1}$)	ERR ^b ($\mu\text{mol}\cdot\text{h}^{-1}$)	CO yield ($\mu\text{mol}\cdot\text{h}^{-1}$)	CH_4 yield ($\mu\text{mol}\cdot\text{h}^{-1}$)	H_2 yield ($\mu\text{mol}\cdot\text{h}^{-1}$)	ERR ^b ($\mu\text{mol}\cdot\text{h}^{-1}$)	CH_4 selectivity ^c (%)
TiO_{2-x}	0.0027	0.0022	0.0230	0.34	0.0818	—	1.3344	45.3
D- TiO_{2-x}	0.0041	0.0018	0.0226	0.6218	0.0336	—	1.5124	17.8
Pt/ TiO_{2-x}	0.0026	0.0034	0.0324	0.1714	0.1298	0.84	3.0612	33.9
Pt/D- TiO_{2-x}	0.0037	0.0048	0.0458	0.0256	0.3412	0.17	3.1352	87.5

^a Reaction conditions: solar light irradiation for 5 h, 20 mg catalyst, 2 mL H_2O , 0.1 MPa CO_2 , temperature of 289 K (room temperature) for the PC process and 393 K for the PTC process.

^b ERR: Electron reaction rate = $2r(\text{H}_2) + 8r(\text{CH}_4) + 2r(\text{CO})$, where r is an empirical rate constant.

^c CH_4 selectivity = $\{[8r(\text{CH}_4)]/[ERR]\} \times 100\%$

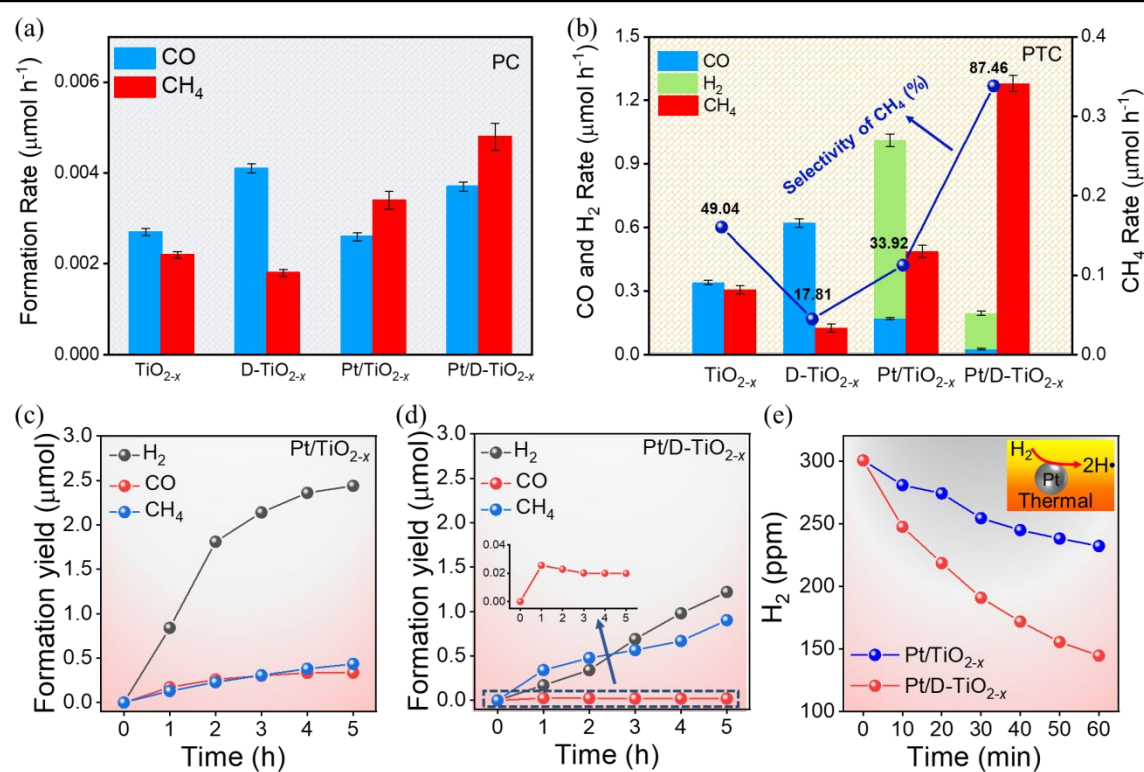


Fig. 6 (a) PC and (b) PTC induced CO_2 to CO conversion using different photocatalysts with and without Pt loading. The results obtained without Pt loading are reproduced here from Fig. 6 for convenience. H_2 , CO, and CH_4 evolution during PTC induced CO_2 conversion with respect to reaction time using (c) Pt/ TiO_{2-x} and (d) Pt/D- TiO_{2-x} . (e) Remaining H_2 obtained with respect to H_2 decomposition time using Pt/ TiO_{2-x} and Pt/D- TiO_{2-x} catalysts under thermally assisted conditions in the absence of light, where the inset illustrates the H_2 splitting process facilitated by Pt nanoparticles.

disordering process effectively improves the charge transport characteristics of TiO_{2-x} .

To explore the relationship between structure and photoactivity, US-X samples were further characterized by XRD, Raman, TEM, XPS and UV-vis spectra, as shown in Fig.S11-S14. From the XRD, Raman, TEM and HRTEM, TiO_{2-x} treated by ultrasonication for different hours had no obvious change in crystal phase and composition (Fig.S11-S12). As observed for XPS spectra of Ti 2p and O 1s, the binding

energies of these peaks shift to higher values with prolonging time of ultrasonication treatment (Fig.S13). It is believed that the shift of binding energy of the Ti 2p and O 1s to a higher value could be attributed to the increased concentration of surface oxygen vacancies. The UV-vis diffuse absorbance spectra of US-X are shown in Fig. S14. The decreased slope correlates with weaker crystallinity, which can be associated with the formation of disordered layer treated by ultrasonication. Moreover, a blue shift in the UV region

and increased absorption in visible region is observed. The blue shift can be explained by the Moss-Burstein effect. The Fermi level is shifted upward when the electron carrier concentration exceeds the DOS at the conduction band edge, which usually corresponds to degenerate doping in semiconductors. The gradually increased optical absorption with the extended ultrasonic time indicates the generation of localized band bending (also named as band tail) in these samples.

3.4.2 CH₄ selectivity before and after Pt loading. Figs. 6a and b respectively present the results of PC and PTC induced CO₂ to CO conversion using the TiO_{2-x} and D-TiO_{2-x} photocatalysts before and after Pt loading. The results for the supports prior to Pt loading are copied here from Fig. 6 to facilitate comparison. In addition, the results obtained for the PC and PTC processes using all photocatalysts considered are itemized in Table 1 for convenience. The results in Fig. 6a indicate that the CO formation rates obtained during PC reduction using either support is largely unaffected by Pt loading. However, the formation rates of CH₄ are clearly increased after Pt loading, particularly for the D-TiO_{2-x} photocatalyst. Here, the CH₄ formation rate using Pt/D-TiO_{2-x} was greater than that obtained using D-TiO_{2-x} by a factor of 2.67, while the CH₄ formation rate using Pt/TiO_{2-x} was greater than that obtained using TiO_{2-x} by a factor of 1.55. Moreover, the CH₄ formation rate using Pt/D-TiO_{2-x} was greater than that obtained using Pt/TiO_{2-x} by a factor of 1.41. These results demonstrate that the combination of Pt deposition and the disordered surface layer facilitates the multi-electron reduction of CO₂, and thereby enhances the CH₄ yield. Nonetheless, the CO and CH₄ formation rates obtained in the PC process using any of the proposed photocatalysts remain quite low.

The results in Fig. 6b show that the products obtained during PTC reduction included CO and CH₄, as well as H₂ under conditions of Pt loading for both supports. We note from the results in the figure for the Pt/D-TiO_{2-x} facilitated process that the CH₄ formation rate increases to 0.3412 μmol·h⁻¹ and the CH₄ selectivity increases to 87.5% from the values of 0.0336 μmol·h⁻¹ and 17.8% respectively obtained using D-TiO_{2-x}. The relative high performance of the PTC process employing the Pt/D-TiO_{2-x} photocatalyst is particularly well illustrated by the fact that the obtained CH₄ formation rate is greater than the corresponding formation rates obtained by the PC process using the Pt/D-TiO_{2-x} and TiO_{2-x} photocatalysts by factors of 71.08 and 155.09, respectively. In fact, the selectivity of CH₄ should be fairly evaluated by consideration of H₂ product. To report a high selectivity, many works neglect the yield of H₂. Herein, we calculated the selectivity of CH₄ by including the products of CO, H₂ and CH₄. The calculation is expressed as following: Selectivity of CH₄ = $r(\text{CH}_4) / \{r(\text{CH}_4) + r(\text{CO}) + r(\text{H}_2)\}$.²⁰ Meanwhile, we compare the selectivity of CH₄ over Pt/D-TiO_{2-x} with other Pt loaded photocatalysts in Table S2. The comparison indicates that both the yield and CH₄ selectivity obtained in this work remain a high level among the presently reported photocatalysts.

The factors leading to the increased CH₄ selectivity of the Pt/D-TiO_{2-x} photocatalyst were further evaluated by monitoring the increasing yields of CO, CH₄, and H₂ obtained in the PTC process with increasing reaction time using Pt/TiO_{2-x} and Pt/D-TiO_{2-x}. These results are respectively given in Figs. 6c and d. Here, we note that the CO, CH₄, and H₂ yields obtained using the Pt/TiO_{2-x} photocatalyst (Fig. 6c) monotonically increased uniformly with increasing reaction time.

However, the CH₄ and H₂ yields monotonically increased non-uniformly while the CO yield decreased slightly with increasing reaction time when using the Pt/D-TiO_{2-x} photocatalyst (Fig. 6d). The different formation rates of the products lead to different product selectivity. According to the experimental results of photothermal catalysis shown in Fig. 6b, decreasing Pt size from 4.06 nm to 2.33 nm works well in enhancing the CH₄ selectivity from 33.92 to 87.46%. This means that decreasing Pt size is a key point in improving the CH₄ selectivity. Furthermore, in comparison with experimental results of photocatalysis shown in Fig. 6a, decreasing Pt size slightly improves the CO and CH₄ yield and the selectivity is hardly increased. This means that, in addition to decreasing Pt size, the thermal assistance does play important role in improving the CH₄ selectivity. By closer observation of the formation rate of products in Fig. 6b, it is found that the H₂ formation rate is sharply decreased from Pt (4.06 nm)/TiO₂ to Pt (2.33 nm)/TiO₂. As is well reported, Pt can serve as a good catalyst for H₂ activation and hydrogen spillover.²¹ Here, to understand the synergistic effect of Pt size and thermal assistance, we trace a thermal activation of H₂ in a mixed N₂/H₂ gas in dark at 393 K. As shown in Fig. 6e, H₂ can be thermally decomposed over Pt/TiO_{2-x} in dark. There is a higher decomposition rate of H₂ over Pt (2.33 nm)/TiO₂ than Pt (4.06 nm)/TiO₂. This demonstrates that integration of effect of thermal and Pt size could promote H₂ splitting to H₂ easily, which is beneficial for the hydrogenation of CO₂ and therefore improvement of the CH₄ selectivity.

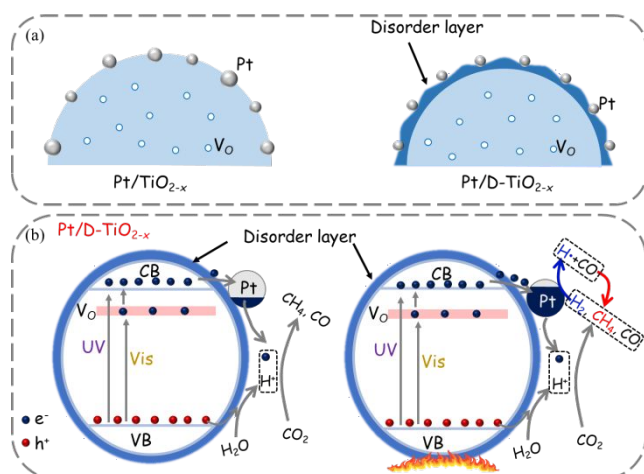
The smaller Pt loaded on D-TiO_{2-x} indeed influence the catalytic conversion of CO₂ and the selectivity of CH₄. Firstly, the smaller Pt loaded on D-TiO_{2-x} can enhance the yield of CH₄.¹⁴ At the same time, the yield of H₂ is also enhanced, which unfortunately decreases the selectivity of CH₄.^{20,54,55} In this work, the effect of Pt size is restudied in photothermal catalytic reduction of CO₂. In detail, thermal coupled photocatalysis reveals a promoted evolution of H₂ side product over Pt (4.06 nm)/TiO₂ (Fig. 6b). Whereas a promoted H₂ splitting over Pt (2.33 nm)/TiO₂ is observed (Fig. 6e), which is seldom reported in conventional Pt/TiO₂ photocatalysis. The synergy of improved charge separation at Pt/TiO₂ interface induced by surface disordering and accelerated H₂ consumption nearby smaller Pt nanoparticles by thermal assistance are believed critically important for simultaneous enhancement of CO₂ conversion rates and CH₄ product selectivity.

The stability of Pt/D-TiO_{2-x} toward CO₂ reduction is evaluated in five cycles and the results are supplemented in Fig. S15. As can be seen, the CH₄ yield had no significant decrease, suggesting the good stability for Pt/D-TiO_{2-x}. In order to verify the stability of Pt nanoparticles, we test the Pt/D-TiO_{2-x} before and after the photothermal catalysis by XPS analysis. From the Pt 4f spectra, there is no obvious shift of binding energy (Fig. S16). This indicates that the Pt nanoparticles are subjected to no oxidation after catalytic test and hence display good stability.

The PC and PTC test results conducted with the TiO_{2-x} and D-TiO_{2-x} photocatalysts both with and without Pt nanoparticle loading support the following conclusions.

- (1) The PTC process outperforms the PC process with respect to the CO₂ to CO conversion rate for all photocatalysts considered.
- (2) Use of the D-TiO_{2-x} photocatalyst significantly increases the formation rate of CO rather than CH₄ in both the PC and PTC processes.

- (3) The integration of oxygen vacancies, surface layer disordering, and Pt nanoparticle deposition selectively promotes CH_4 formation, particularly in the PTC process.



Scheme 1 (a) Models of Pt/TiO_{2-x} and Pt/D-TiO_{2-x} nanocatalysts with Pt nanoparticles of varying sizes and degrees of dispersion over the nano-support surfaces. (b) Schematics illustrating the fundamental mechanisms of PC and PTC reactions using Pt/TiO_{2-x} and Pt/D-TiO_{2-x} nanocatalysts.

3.5 Proposed mechanisms facilitating enhanced CH₄ selectivity

Based on the above results and discussion, we propose the Pt/TiO_{2-x} and Pt/D-TiO_{2-x} models shown in Scheme 1a. Firstly, the disordered surface layer of D-TiO_{2-x} facilitates the photodeposition of Pt nanoparticles with a narrower size distribution and smaller average size than those obtained on the TiO_{2-x} surface, and the Pt nanoparticles are more widely dispersed over the surface of D-TiO_{2-x} because the disordered layer produces a high density of active sites that promotes the wide dispersion of Pt nanoparticles. Meanwhile, Scheme 1b illustrates that the coupling of thermal energy with the PC process increases the rate of electron and hole transfer to the Pt nanoparticles at the surface of the supports, resulting in the increased formation rates of products. Moreover, the thermal energy in the PTC process assists in the splitting of H₂ molecules by the Pt nanoparticles, which thereafter facilitates the reaction between monatomic H with CO. Scheme 1b further illustrates how multiple factors work together synergistically in the proposed PTC system to promote rapid CO₂ reduction, low H₂ formation, and high CH₄ selectivity. These can be specified as follows.

(1) Increased charge carrier transfer to the surface is facilitated by the enhanced generation of electrons and holes via thermal activation while their lifetimes are enhanced by the disordered layer in conjunction with Pt nanoparticle loading via reduced charge carrier recombination.

(2) The disordered layer of D-TiO_{2-x} promotes the wide dispersion of Pt nanoparticles, while also ensuring that the Pt nanoparticles are composed of fully reduced metallic Pt atoms in the Pt⁰ state.

(3) Thermal energy promotes the rapid decomposition of molecular H₂ to monatomic H by the catalytic activity of the fully metallic Pt nanoparticles.

4. Conclusion

In summary, we have developed an efficient photothermal catalytic system that promotes rapid CO₂ reduction, low H₂ formation, and high CH₄ selectivity by coupling thermal energy with an advanced surface engineered Pt/TiO_{2-x} photocatalyst with oxygen vacancies. Here, disordering has been induced in the surface layer of TiO_{2-x} by a high-power ultrasonic treatment and highly dispersed Pt nanoparticles have also been loaded on the surface. Comprehensive analysis revealed that the surface disordering decreased the average size of the Pt nanoparticles from 4.06 to 2.33 nm, resulting in improved charge carrier separation and increased carrier lifetimes. The adoption of the as-fabricated Pt/D-TiO_{2-x} photocatalyst in the thermally assisted process conducted at 393 K provided a CH₄ formation rate that was greater than that obtained by the standard photocatalytic process conducted at room temperature using the TiO_{2-x} photocatalyst by a factor of 155. Meanwhile, the proposed photothermal catalytic system provided a CH₄ selectivity of 87.5%. The superior performance of the proposed system was argued to result from the multiple factors of thermal assistance, oxygen vacancies, surface disorder, and Pt nanoparticle loading that work together synergistically. This work represents a proven strategy for the design of highly efficient photothermal catalysts that enhance the yield and selectivity of CH₄ in the CO₂ reduction process.

Conflicts of interest

There are no conflicts to declare.

Acknowledgements

This work was supported by the Natural Science Foundation of China (91833303, 51072032, 51102001 and 51872044), Jilin Province Science and Technology Development Project (20180101175JC), and the 111 project (No. B13013). TEM characterization and analysis were supported by the U.S. Department of Energy (DOE), Office of Science, Basic Energy Sciences (BES), under Award # 67037. Electron traps density measured by RDB-PAS technology was supported by Professor Bunsho Ohtani from Graduate School of Environmental Science, Hokkaido University.

Notes and references

- J. Jia, C. Qian, Y. Dong, Y. F. Li, H. Wang, M. Ghossoub, K. T. Butler, A. Walsh and G. A. Ozin, *Chem. Soc. Rev.*, 2017, **46**, 4631–4644.
- G. Chen, G. I. N. Waterhouse, R. Shi, J. Zhao, Z. Li, L.-Z. Wu, C.-H. Tung and T. Zhang, *Angew. Chemie Int. Ed.*, 2019, **58**, 17528–17551.
- W. Kim, B. A. McClure, E. Edri and H. Frei, *Chem. Soc. Rev.*, 2016, **45**, 3221–3243.
- J. Ran, M. Jaroniec and S.Z. Qiao, *Adv. Mater.*, 2018, **30**, 1704649.
- J. Jin, J. Yu, D. Guo, C. Cui and W. Ho, *Small*, 2015, **11**, 5262–5271.
- G. Yin, X. Huang, T. Chen, W. Zhao, Q. Bi, J. Xu, Y. Han and F. Huang, *ACS Catal.*, 2018, **8**, 1009–1017.
- Y. X. Pan, Y. You, S. Xin, Y. Li, G. Fu, Z. Cui, Y. L. Men, F. F. Cao, S.

- H. Yu and J. B. Goodenough, *J. Am. Chem. Soc.*, 2017, **139**, 4123–4129.
- 8 Q. Lang, Y. Yang, Y. Zhu, W. Hu, W. Jiang, S. Zhong, P. Gong, B. Teng, L. Zhao and S. Bai, *J. Mater. Chem. A*, 2017, **5**, 6686–6694.
- 9 Y. Liu, Z. Zhang, Y. Fang, B. Liu, J. Huang, F. Miao, Y. Bao and B. Dong, *Appl. Catal., B*, 2019, **252**, 164–173.
- 10 D. Dong, C. Yan, J. Huang, N. Lu, P. Wu, J. Wang and Z. Zhang, *J. Mater. Chem. A*, 2019, **7**, 24180–24185.
- 11 Z. Jiang, Y. Li, Q. Zhang, Y. Yang, S. Wu, J. Wu and X. Zhao, *J. Mater. Chem. A*, 2019, **7**, 4881–4892.
- 12 U. Ulmer, T. Dingle, P. N. Duchesne, R. H. Morris, A. Tavasoli, T. Wood and G. A. Ozin, *Nat. Commun.*, 2019, **10**, 3169.
- 13 Y. Li, J. Hao, H. Song, F. Zhang, X. Bai, X. Meng, H. Zhang, S. Wang, Y. Hu and J. Ye, *Nat. Commun.*, 2019, **10**, 2359.
- 14 Y. Liu, C. Miao, P. Yang, Y. He, J. Feng and D. Li, *Appl. Catal., B*, 2019, **244**, 919–930.
- 15 X. Pan, M. Q. Yang, X. Fu, N. Zhang and Y. J. Xu, *Nanoscale*, 2013, **5**, 3601–3614.
- 16 G. Yin, Q. Bi, W. Zhao, J. Xu, T. Lin and F. Huang, *ChemCatChem*, 2017, **9**, 4389–4396.
- 17 B. Wang, X. Wang, L. Lu, C. Zhou, Z. Xin, J. Wang, X. K. Ke, G. Sheng, S. Yan and Z. Zou, *ACS Catal.*, 2018, **8**, 516–525.
- 18 Y. Li, C. Wang, M. Song, D. Li, X. Zhang and Y. Liu, *Appl. Catal., B*, 2019, **243**, 760–770.
- 19 W. N. Wang, W. J. An, B. Ramalingam, S. Mukherjee, D. M. Niedzwiedzki, S. Gangopadhyay and P. Biswas, *J. Am. Chem. Soc.*, 2012, **134**, 11276–11281.
- 20 C. Dong, C. Lian, S. Hu, Z. Deng, J. Gong, M. Li, H. Liu, M. Xing and J. Zhang, *Nat. Commun.*, 2018, **9**, 1252.
- 21 C. W. Y. Wang, J. Zhao, Y. Li, *Appl. Catal. B Environ.*, 2018, **226**, 544–553.
- 22 J. Jin, C. Wang, X. N. Ren, S. Z. Huang, M. Wu, L. H. Chen, T. Hasan, B. J. Wang, Y. Li and B. L. Su, *Nano Energy*, 2017, **38**, 118–126.
- 23 Y. Yang, P. Gao, X. Ren, L. Sha, P. Yang, J. Zhang, Y. Chen and L. Yang, *Appl. Catal., B*, 2017, **218**, 751–757.
- 24 Z. Lian, W. Wang, G. Li, F. Tian, K. S. Schanze and H. Li, *ACS Appl. Mater. Interfaces*, 2017, **9**, 16959–16966.
- 25 J. Wang, Y. Li, L. Deng, N. Wei, Y. Weng, S. Dong, D. Qi, J. Qiu, X. Chen and T. Wu, *Adv. Mater.*, 2017, **29**, 1603730.
- 26 H. Tan, Z. Zhao, M. Niu, C. Mao, D. Cao, D. Cheng, P. Feng and Z. Sun, *Nanoscale*, 2014, **6**, 10216–10223.
- 27 J. H. P. K. Zhang, L. Wang, J. K. Kim, M. Ma, G. Veerappan, C. L. Lee, K. Kong, H. Lee, *Energy Environ. Sci.*, 2016, **9**, 499–503.
- 28 P. Yan, G. Liu, C. Ding, H. Han, J. Shi, Y. Gan and C. Li, *ACS Appl. Mater. Interfaces*, 2015, **7**, 3791–3796.
- 29 L. Lin, J. Huang, X. Li, M. A. Abass and S. Zhang, *Appl. Catal., B*, 2017, **203**, 615–624.
- 30 C. Wang, X. Zhang and Y. Liu, *Nanoscale*, 2014, **6**, 5329–5337.
- 31 C. Fan, C. Chen, J. Wang, X. Fu, Z. Ren, G. Qian and Z. Wang, *Sci. Rep.*, 2015, **5**, 11712.
- 32 C. Fan, X. Fu, L. Shi, S. Yu, G. Qian and Z. Wang, *J. Alloys Compd.*, 2017, **703**, 96–102.
- 33 J. H. Bang and K. S. Suslick, *Adv. Mater.*, 2010, **22**, 1039–1059.
- 34 H. Xu, B. W. Zeiger and K. S. Suslick, *Chem. Soc. Rev.*, 2013, **42**, 2555–2567.
- 35 W. Song, S. Ma, L. Wang, J. Liu and Z. Zhao, *ChemCatChem*, 2017, **9**, 4340–4344.
- 36 L. Wang, W. Song, J. Deng, H. Zheng, J. Liu, Z. Zhao, M. Gao and Y. Wei, *Nanoscale*, 2018, **10**, 6024–6038.
- 37 P. Ferrari, K. Hansen, P. Lievens and E. Janssens, *Phys. Chem. Chem. Phys.*, 2018, **20**, 29085–29090.
- 38 Y. Chimupala, P. Junploy, T. Hardcastle, A. Westwood, A. Scott, B. Johnson and R. Brydson, *J. Mater. Chem. A*, 2016, **4**, 5685–5699.
- 39 I. Nakamura, N. Negishi, S. Kutsuna, T. Ihara, S. Sugihara and K. Takeuchi, *J. Mol. Catal. A Chem.*, 2000, **161**, 205–212.
- 40 G. Cappelletti, S. Ardizzone, C. L. Bianchi, S. Gialanella, A. Naldoni, C. Pirola and V. Ragaini, *Nanoscale Res. Lett.*, 2009, **4**, 97–105.
- 41 L. Kong, Z. Jiang, C. Wang, F. Wan, Y. Li, L. Wu, J. F. Zhi, X. Zhang, S. Chen and Y. Liu, *ACS Appl. Mater. Interfaces*, 2015, **7**, 7752–7758.
- 42 Y. Zhao, Y. Zhao, R. Shi, B. Wang, G. I. N. Waterhouse, L. Wu, C. Tung and T. Zhang, *Adv. Mater.*, 2019, **31**, 1806482.
- 43 S. Chen, H. Wang, Z. Kang, S. Jin, X. Zhang, X. Zheng, Z. Qi, J. Zhu, B. Pan and Y. Xie, *Nat. Commun.*, 2019, **10**, 788.
- 44 B. Santara, P. K. Giri, K. Imakita and M. Fujii, *Nanoscale*, 2013, **5**, 5476–5488.
- 45 L. Kong, C. Wang, H. Zheng, X. Zhang and Y. Liu, *J. Phys. Chem. C*, 2015, **119**, 16623–16632.
- 46 C. S. Granerød, S. R. Bilden, T. Aarholt, Y.-F. Yao, C. C. Yang, D. C. Look, L. Vines, K. M. Johansen and Ø. Prytz, *Phys. Rev. B*, 2018, **98**, 115301.
- 47 J. Wang, P. Liu, X. Fu, Z. Li, W. Han and X. Wang, *Langmuir*, 2009, **25**, 1218–1223.
- 48 Y. Yang, G. Liu, J. T. S. Irvine and H.-M. Cheng, *Adv. Mater.*, 2016, **28**, 5850–5856.
- 49 L. Li, J. Yan, T. Wang, Z.-J. Zhao, J. Zhang, J. Gong and N. Guan, *Nat. Commun.*, 2015, **6**, 5881.
- 50 W. Zhou, W. Li, J. Q. Wang, Y. Qu, Y. Yang, Y. Xie, K. Zhang, L. Wang, H. Fu and D. Zhao, *J. Am. Chem. Soc.*, 2014, **136**, 9280–9283.
- 51 Y. Zhao, Y. Wei, X. Wu, H. Zheng, Z. Zhao, J. Liu and J. Li, *Appl. Catal., B*, 2018, **226**, 360–372.
- 52 A. Nitta, M. Takashima, N. Murakami, M. Takase and B. Ohtani, *Electrochim. Acta*, 2018, **264**, 83–90.
- 53 A. Nitta, M. Takashima, M. Takase and B. Ohtani, *Catal. Today*, 2019, **321**, 2–8.
- 54 Z. Xiong, Z. Lei, C. Kuang, X. Chen, B. Gong, Y. Zhao, J. Zhang, C. Zheng and J. C. S. Wu, *Appl. Catal., B*, 2017, **202**, 695–703.
- 55 M. Borges Ordoniño and A. Urakawa, *J. Phys. Chem. C*, 2019, **123**, 4140–4147.

TOC

Ultrasonic disordering of TiO_2 surface prefers smaller Pt nanoparticles and promotes thermal-assisted photocatalytic reduction of CO_2 for high CH_4 selectivity.

